PROCEEDINGS A

rspa.royalsocietypublishing.org

Research

Cite this article: Renzi E. 2016 Hydroelectromechanical modelling of a piezoelectric wave energy converter. *Proc. R. Soc. A* **472**: 20160715.
http://dx.doi.org/10.1098/rspa.2016.0715

Received: 20 September 2016
Accepted: 28 October 2016

Subject Areas:
ocean engineering, civil engineering

Keywords:
wave energy, wave–structure interaction, hydroelectromechanical resonance, piezoelectricity

Author for correspondence:
E. Renzi
e-mail: e.renzi@lboro.ac.uk

Hydroelectromechanical modelling of a piezoelectric wave energy converter

E. Renzi

Department of Mathematical Sciences, Loughborough University, Leics LE11 3TU, UK

ER, 0000-0002-1459-5565

We investigate the hydroelectromechanical-coupled dynamics of a piezoelectric wave energy converter. The converter is made of a flexible bimorph plate, clamped at its ends and forced to motion by incident ocean surface waves. The piezoceramic layers are connected in series and transform the elastic motion of the plate into useful electricity by means of the piezoelectric effect. By using a distributed-parameter analytical approach, we couple the linear piezoelectric constitutive equations for the plate with the potential-flow equations for the surface water waves. The resulting system of governing partial differential equations yields a new hydroelectromechanical dispersion relation, whose complex roots are determined with a numerical approach. The effect of the piezoelectric coupling in the hydroelastic domain generates a system of short- and long-crested weakly damped progressive waves travelling along the plate. We show that the short-crested flexural wave component gives a dominant contribution to the generated power. We determine the hydroelectromechanical resonant periods of the device, at which the power output is significant.

1. Introduction

The wave energy industry has recently suffered from major pitfalls that highlighted the shortcomings of several concepts to extract energy from the motion of the ocean [1,2]. Among the reasons of such failures are the sheer size and complexity of the proposed devices, and the use of costly design components (e.g. materials, underwater moving parts) to resist the wave action. These factors concur to make the levelized cost of energy (LCOE) of wave energy converters (WECs) not yet competitive against that of fossil fuels [3].

THE ROYAL SOCIETY PUBLISHING

To improve this scenario, new research efforts must focus on innovative ideas, which make use of sleek design and smart materials to generate useful electricity at a much smaller LCOE than that of existing devices. One of such ideas is to use piezoelectric materials, which are able to establish a voltage upon application of an external stress. A piezoelectric WEC (PWEC) exploits the natural cycles of stresses and strains induced by the wave motion to generate an output AC voltage [4]. The estimated power potential of a typical PWEC is in the order of watts to kilowatts. This is enough to supply appliances (e.g. LEDs, wireless routers, PCs), ocean buoys and sensors. Despite being less powerful than other WECs (e.g. the nominal capacity of an oscillating wave surge converter is in the order of hundreds of kilowatts; see [5–7]), PWECs enjoy the significant advantages of being low maintenance and versatile. For example, they can also be employed to increase wave damping around offshore oil platforms and in combination with near shore breakwaters [4].

Although ambient power harvesting through piezoelectricity has a long and honourable history [8], its application to ocean energy conversion has been proposed only in the past few years. Novel PWEC concepts include cantilevered beams [9,10] and piezoelectric buoys [11]. So far, such devices have been studied with rather simplified mathematical models, in which the effect of the piezoelectric layers on the dynamic response of the system was neglected. The bending force resulting from the action of the waves on the structure was plugged separately into the electric circuit equations to estimate the voltage on the piezoelectric layers [9–11]. With that simplified approach, the hydroelectromechanical problem was in fact uncoupled into two separate wave structure and electric problems. Such an approximate analysis is useful to obtain a preliminary estimate of the extracted power, but cannot be trusted to provide accurate results. Indeed, in reality, the dynamics of waves, structural elasticity and piezoelectricity are inherently coupled in a PWEC, and so the development of a hydroelectromechanical model is fundamental to providing an accurate analysis of the system.

In this paper, we analyse the coupled hydroelectromechanical dynamics of a piezoelectric plate WEC. The idea of using a flexible plate to extract energy from the waves was first introduced by Koola & Ibragimov [12], though they did not model any power take-off mechanism, and is inspired by nature. It is long known that spreading a thin film of oil on the sea surface has the effect of calming troubled waters. For example, this practice was used by ancient sailors, as described by Franklin [13]. Later, Lamb showed that the tension variations at the oil–water interface 'produce an alternating tangential drag on the water, with a consequent increase in the rate of dissipation of energy' [14]. Similarly, a piezoelectric plate WEC can extract energy from the ambient wave motion by converting tension variations at the plate–water interface into a voltage, owing to the piezoelectric effect. This, in turn, exerts a damping action on the waves. Piezoelectric plates have already been considered for the task of extracting energy from currents. For example, Doaré & Michelin [15,16] developed a coupled model of energy extraction from piezoelectric flags fluttering in an axial flow. However, to the best of our knowledge, no coupled models of wave energy extraction from piezoelectric plates have been developed yet.

We consider the power generation by a bimorph piezoelectric plate in ocean surface waves of varying frequency. We derive a novel hydroelectromechanical dispersion relation for the flexural waves propagating on the plate. The piezoelectric coupling in the hydroelastic domain generates a system of short- and long-crested weakly damped progressive waves travelling along the plate. We show that the short-crested flexural wave component gives a dominant contribution to the generated power. We determine new hydroelectromechanical resonant periods at which the power output of the device is significant.

This paper is organized as follows. First, we introduce the governing equations of the coupled system by using a distributed-parameter approach for the piezoelectric plate and a potential-flow theory for the waves (§2). Then, we solve the coupled system of partial differential equations by means of domain decomposition and the method of matching potentials (§3). After that, we analyse the mechanism of wave power extraction by the device (§4) and discuss the behaviour of a typical configuration of the piezoelectric plate WEC (§5). Conclusions and suggestions for further work are finally presented (see §6).

2. Governing equations

Referring to figure 1, define a global coordinate system (x', y', z'), with the z'-axis pointing upwards from the undisturbed water level $z' = 0$. The x'-axis is directed along the direction of propagation of incoming surface waves of amplitude A' and angular frequency ω'. Variables with primes denote physical quantities. The bottom of the ocean is located at a constant depth $z' = -h'$ and the piezoelectric converter is a flexible plate, clamped at both ends at $(x', z') = (\pm L', -d')$. As is usual in structural dynamics [17], we introduce a local reference system on the plate, with $(X', Y', Z') = (x', -y', -z' - d')$, so that the local Z' axis points downwards (see again figure 1). In this section, we shall first derive a distributed-parameter model for the governing equations of the piezoelectric plate in the local reference system. Then, we shall couple the model equations of the plate with those of the surface waves, based on a potential-flow theory, in the global reference system.

(a) Distributed-parameter modelling of the piezoelectric plate

Consider a flexible plate whose width in the transverse Y'-direction is much greater than its length $2L'$ along the X'-axis. Hence, the deformations of the plate will be modelled as purely two-dimensional, i.e. $\partial/\partial Y' = 0$. Consider a bimorph configuration of the plate, in which piezoelectric layers are perfectly bonded to both faces of a flexible substrate, with opposite polarities in the Z'-direction, as shown in figure 2. Such a symmetric bimorph configuration is also used in the design of cantilevered piezoelectric energy harvesters from ambient vibrations; see [8]. Electrodes of negligible thickness cover the top and the bottom faces of each piezoelectric layer and ensure that a potential difference is established across them. We assume that the deformations are small and that the behaviour of the structure is linear elastic. The piezoelectric layers are homogeneous and have thickness d_{p}', Young's modulus E_{p}' (in N m^{-2}) and Poisson's ratio ν_{p}. The piezoelectric layers are made of discrete piezoelectric patches, each of length $\mathrm{d}X' \ll L'$. The patches are arranged one after another to cover both sides of the substrate [8,15]. The elastic substrate is homogeneous and has thickness d_0', Young's modulus E_0' and Poisson's ratio ν_0. From now on, primes will be dropped for simplicity in this section. Because the system is homogeneous, the vertical displacement $W(X, t)$, the stresses $\sigma_{ij}(X, Z, t)$, with $i, j = X, Y, Z$, the strains $\epsilon_{ij}(X, Z, t)$ and the voltage $V(X, t)$ are continuous along the plate. Hence, the converter can be modelled as a uniform composite plate based on the Kirchhoff plate theory [17].

Consider the cylindrical bending of a plate element of unit width and length $\mathrm{d}X \ll L$, under the action of a vertical surface load $\tilde{q}(X, t)$ (in N m^{-2}). The equation of motion of the plate element in the local coordinate system of figure 2 is

$$\frac{\partial^2 M_{XX}}{\partial X^2} - I_{\mathrm{b}} \frac{\partial^2 W}{\partial t^2} = -\tilde{q}, \tag{2.1}$$

(see [17]) where

$$M_{XX} = \int_{-d_{\mathrm{b}}/2}^{d_{\mathrm{b}}/2} \sigma_{XX} Z \, \mathrm{d}Z \tag{2.2}$$

is the internal bending moment per unit width (in N), $d_{\mathrm{b}} = d_0 + 2d_{\mathrm{p}} \ll L$ is the total thickness of the bimorph and

$$I_{\mathrm{b}} = \int_{-d_{\mathrm{b}}/2}^{d_{\mathrm{b}}/2} \rho(Z) \, \mathrm{d}Z = \rho_0 d_0 + 2\rho_{\mathrm{p}} d_{\mathrm{p}} \tag{2.3}$$

is the surface density of the bimorph (in kg m^{-2}). In (2.3), ρ_{p} is the density of the piezoelectric layers and ρ_0 is the density of the substrate. We consider isotropic materials, so that the

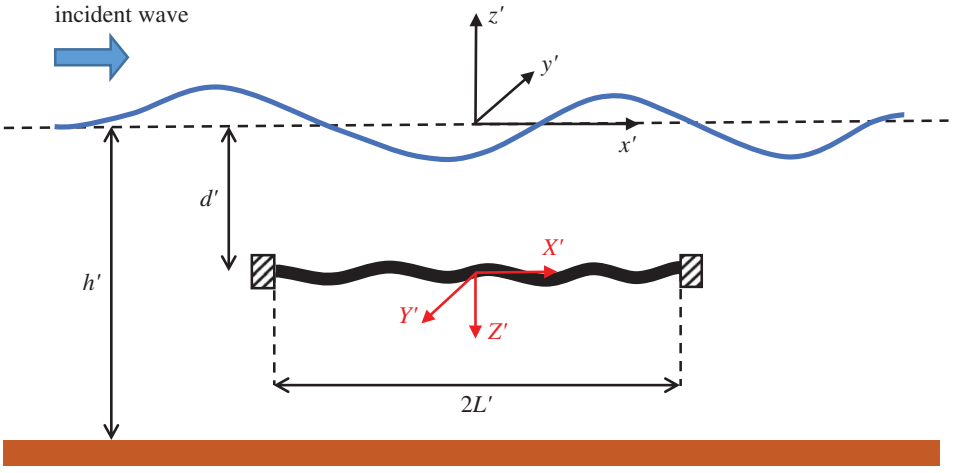

Figure 1. Geometry of the system in physical variables. The local reference system on the plate is (X', Y', Z') and the global coordinate system is (x', y', z'). The plate is $2L'$ long and is clamped at both ends at a depth of d' in an ocean of constant depth of h'. (Online version in colour.)

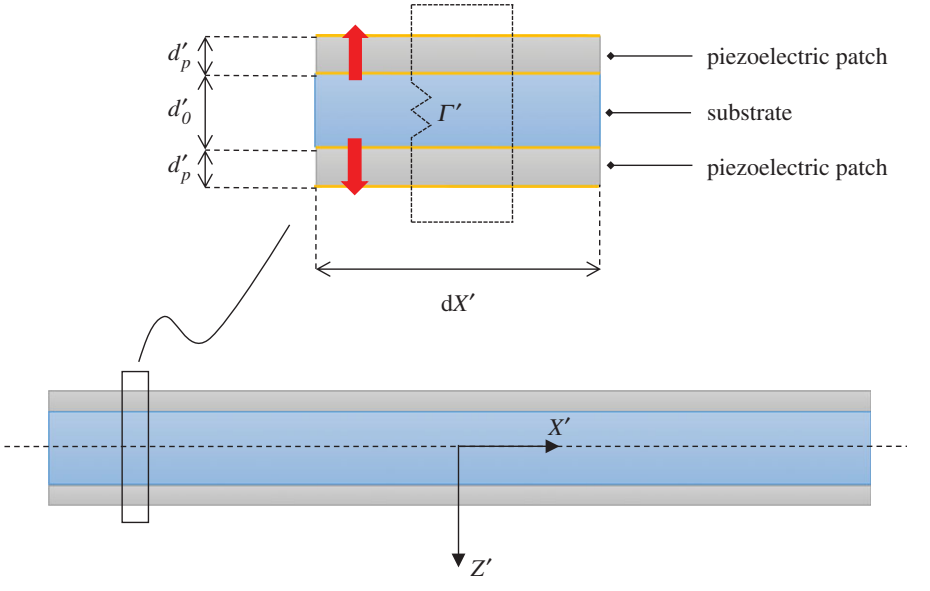

Figure 2. Geometry of the piezoelectric plate and detail of the bimorph configuration for an element of length $dX' \ll L'$, corresponding to the length of a piezoelectric patch. The bold vertical arrows indicate the poling direction of the piezoelectric layers (from negative to positive pole). Electrodes of negligible thickness cover both faces of each piezoelectric patch. Each pair of piezoelectric patches are shunted with an external resistance $1/\Gamma'$, thus powering a resistive circuit. (Online version in colour.)

constitutive linear elastic equation for the substrate is

$$\sigma_{XX} = \frac{E_0}{1-\nu_0^2}\,\epsilon_{XX}. \tag{2.4}$$

Now, we define the 1-, 2-, 3-axes of piezoelectricity and couple them with the material X-, Y- and Z-directions, respectively. The piezoelectric constitutive equations for the layers are

$$\sigma_{XX} = \frac{E_\mathrm{p}}{1-\nu_\mathrm{p}^2}\epsilon_{XX} - \frac{E_\mathrm{p}\, d_{31}}{1-\nu_\mathrm{p}} E_3 \tag{2.5}$$

and

$$D_3 = \frac{E_\mathrm{p} d_{31}}{1-\nu_\mathrm{p}} \epsilon_{XX} + \epsilon^S E_3. \tag{2.6}$$

In the latter, $E_3(X,t)$ is the vertical component of the electric field $\mathbf{E}$ (in V m^{-1}), $D_3(X,t)$ is the vertical component of the electric displacement $\mathbf{D}$ (in C m^{-2}), ϵ^S is the permittivity of the piezoceramic at constant strain (in F m^{-1}) and d_{31} is the piezoelectric coupling constant (in m V^{-1}); see [8]. Because the electrodes are aligned along the horizontal X-direction, the electric field and electric displacement are both aligned along the vertical Z-direction [18]. Note that the sign of d_{31} is opposite for the top ($d_{31} < 0$) and bottom ($d_{31} > 0$) piezoelectric layers, according to the relevant poling directions (see again figure 2).

In the absence of axial displacements, $\epsilon_{XX} = -Z\partial^2 W/\partial X^2$. Now, substitute the latter expression into (2.4)–(2.5). Then, substitute the resulting equations into (2.2) and integrate over the thickness of the plate to get

$$M_{XX} = -B\frac{\partial^2 W}{\partial X^2} - \frac{E_\mathrm{p}|d_{31}|}{1-\nu_\mathrm{p}}(d_0 + d_\mathrm{p})E_3 d_\mathrm{p}, \tag{2.7}$$

where

$$B = \frac{E_0 d_0^3}{12(1-\nu_0^2)} + \frac{2E_\mathrm{p} d_\mathrm{p}}{1-\nu_\mathrm{p}^2}\left(\frac{d_0^2}{4} + \frac{d_0\, d_\mathrm{p}}{2} + \frac{d_\mathrm{p}^3}{3}\right) \tag{2.8}$$

is the flexural rigidity of the bimorph. Because the piezoelectric layers are connected in series (see again figure 2), the voltage across the electrodes of each piezoceramic layer is the same. For the top layer, $V_\mathrm{p} = -\int_+^- \mathbf{E}\cdot \mathrm{d}\mathbf{X} = -E_3 d_\mathrm{p}$, so that the total voltage is $V(X,t) = 2V_\mathrm{p} = -2E_3 d_\mathrm{p}$; see [18]. Substitution of the latter expression into (2.7) yields the coupled electromechanical equation

$$M_{XX} = -B\frac{\partial^2 W}{\partial X^2} + \theta V, \tag{2.9}$$

where

$$\theta = \frac{E_\mathrm{p}|d_{31}|}{1-\nu_\mathrm{p}}\frac{d_0 + d_\mathrm{p}}{2}$$

is a piezoelectric coupling factor (in N V^{-1} or, equally, in C m^{-1}).

Now, we need to pair (2.9) with the electrical circuit equations, which describe the power take-off (PTO) mechanism of the converter. Following a common practice in modelling vibration-based energy harvesters, we model the PTO for each elementary stripe of length dX by shunting the piezoelectric patches with a resistance [15]. Hence, each piezoelectric pair powers a resistive circuit (see again figure 2). As a result of the Gauss law, the electric charge $\Theta(X,t)$ developed in each piezoelectric layer is given by the integral of the electric displacement $\mathbf{D}$ over a surface S of unit width and outward normal $\mathbf{n}(X,Z)$ enclosing an electrode,

$$\Theta = \oint_S \mathbf{D}\cdot\mathbf{n}\,\mathrm{d}S = \int_A D_3\,\mathrm{d}A, \tag{2.10}$$

where A is the electrode area; see [8,18]. Note that the only contribution to the integrand in (2.10) comes from D_3, because $\mathbf{D}$ is oriented along the 3-axis. According to our distributed-parameter approach, we now derive the electrical circuit equations for a generic piezoelectric element of length $\mathrm{d}X \ll L$ and unit width, in which the instantaneous electric field, displacement and voltage are uniform. Differentiating (2.10) over the elementary area dA, using the second piezoelectric relation (2.6) for D_3 and substituting $E_3 = -V/(2d_\mathrm{p})$ gives

$$Q = \frac{E_\mathrm{p} d_{31}}{1-\nu_\mathrm{p}}\epsilon_{XX} - CV. \tag{2.11}$$

In the latter, $Q(X,t) = \mathrm{d}\Theta/\mathrm{d}A$ is the charge per unit area of the piezoelectric layer and $C = \epsilon^S/(2d_\mathrm{p})$ is the electrical surface capacitance (in F m^{-2}); see [18]. Finally, substitution of $\epsilon_{XX} = -Z\partial^2 W/\partial X^2$

into (2.11) and further integration along Z over any of the piezoelectric patches yields the sought electromechanical equation

$$Q = -\theta \frac{\partial^2 W}{\partial X^2} - CV. \tag{2.12}$$

The latter shows that each piezoelectric layer is acting as a parallel-plate capacitor connected in series with the resistance [18]. Now, note that our system is still undetermined, as we have four unknowns (Q, V, W, M_{XX}), but only three equations, namely (2.1), (2.9) and (2.12). One last equation is needed to close the system, and that is indeed Ohm's resistive law: $\partial\Theta/\partial t = \Gamma V$, where $\Gamma = 1/R$ is the conductance and R is the resistive load of the circuit (in S^{-1}). Differentiating Ohm's law over the elementary area $\mathrm{d}A$, in which V is constant, we get

$$\frac{\partial Q}{\partial t} = GV, \tag{2.13}$$

where $G = \mathrm{d}\Gamma/\mathrm{d}A$ is the surface conductance (in $\mathrm{S\ m}^{-2}$). Expressions (2.1), (2.9), (2.12) and (2.13) are the sought electromechanical equations which govern the dynamics of the bimorph. They are similar to the continuous form of the discrete equations derived by [15] and to the system obtained in the Laplace space by [19].

The governing differential equations must be accompanied by appropriate boundary conditions. Because the plate is clamped at both ends, we have

$$W(\pm L, t) = \left.\frac{\partial W(X,t)}{\partial X}\right|_{X=\pm L} = 0. \tag{2.14}$$

If now the plate is immersed in water waves, the dynamic surface load $\tilde{q}(X,t)$ of (2.1) is precisely the pressure forcing applied by the wave field on the plate. Hence, the electromechanical equations need to be coupled with a hydrodynamic system, which is derived in the next section.

(b) Potential-flow modelling of the ocean surface waves

In this section, we derive the governing equations of the hydrodynamic problem in the global reference system (x', y', z'). Use of primes to denote physical quantities is reintroduced from now on. Accordingly, unprimed variables will denote non-dimensional values. We assume that the clamps at the end of the plate do not have any significant effect on the wave field. Within the framework of a linearized potential flow theory, the fluid is inviscid and incompressible and the flow is irrotational. Hence, there exists a velocity potential $\Phi'(x', z', t')$ that satisfies the Laplace equation

$$\nabla'^2 \Phi' = 0 \tag{2.15}$$

in the fluid domain, the kinematic–dynamic boundary condition on the free surface

$$\frac{\partial^2 \Phi'}{\partial t'^2} + g\frac{\partial \Phi'}{\partial z'} = 0, \quad z' = 0, \tag{2.16}$$

where g is the acceleration owing to gravity, the Bernoulli equation

$$gz' + \frac{P'}{\rho} + \frac{\partial \Phi'}{\partial t'} = 0 \tag{2.17}$$

in the fluid domain, where P' is the total pressure and ρ is the density of the ocean, and the no-flux condition at the bottom,

$$\frac{\partial \Phi'}{\partial z'} = 0, \quad z' = -h'. \tag{2.18}$$

Finally, Φ' also needs to satisfy a kinematic condition on the surface of the plate. Let λ' be the characteristic wavelength of the incident waves. Assume that such a wavelength is comparable to the total length of the device, $\lambda'/(2L') = O(1)$. Because the total thickness of the plate $d'_{\mathrm{b}} \ll 2L' \sim \lambda'$,

we can apply the thin-plate hypothesis and consider the thickness of the plate to be immaterial in solving the potential-flow problem; see [5]. This yields the kinematic condition

$$\frac{\partial W'}{\partial t'} = \frac{\partial \Phi'}{\partial z'}, \quad |x'| \le L', \quad z' = d' \pm \delta', \quad \delta' \to 0. \tag{2.19}$$

3. Solution of the coupled system

We are now in a position to couple the electromechanical and the hydrodynamic problems. With this aim, first replace the surface load in (2.1) with the pressure forcing of the waves

$$\tilde{q}'(X', t') = P'(X', -d' + \delta', t') - P'(X', -d' - \delta', t') = P'_+ - P'_-, \quad \delta' \to 0. \tag{3.1}$$

Then, substitute the electromechanical equations (2.9) and (2.12) into the equation of motion (2.1) and rewrite the result in the global reference system (x', z') to obtain

$$\left(B' + \frac{\theta'^2}{C'}\right)\frac{\partial^4 W'}{\partial x'^4} + I'_{\mathrm{b}}\frac{\partial^2 W'}{\partial t'^2} - \frac{\theta'}{C'}\frac{\partial^2 Q'}{\partial x'^2} = \Delta P'. \tag{3.2}$$

In the latter, W' is now defined positive upwards and $\Delta P'(x', t') = P'_- - P'_+$ is the pressure jump across the plate in the z'-direction. Hence, (3.2) is a coupled hydroelectromechanical equation. The electromechanical equation (2.12) and the circuit equation (2.13) in the global reference system are

$$Q' = C'V' + \theta'\frac{\partial^2 W'}{\partial x'^2} \tag{3.3}$$

and

$$V' + \frac{1}{G}\frac{\partial Q'}{\partial t'} = 0, \tag{3.4}$$

respectively (note that E' and V' change sign when expressed in the global coordinates).

Let us now introduce the following non-dimensional variables:

$$\left.\begin{aligned} &(x', y', z', h', d') = L'(x, y, z, h, d), \quad t' = \sqrt{\frac{L'}{g}}\,t, \quad \Phi' = \sqrt{gL'}A'\Phi, \quad P' = \rho g A' P \\ \text{and} \quad &Q' = A'\sqrt{\frac{gI'_{\mathrm{b}}C'}{L'}}\,Q, \quad V' = A'\sqrt{\frac{gI'_{\mathrm{b}}}{L'C'}}\,V, \quad W' = A'W. \end{aligned}\right\} \tag{3.5}$$

Upon substitution of (3.5), the coupled hydroelectromechanical equation of motion (3.2) becomes

$$\beta(1 + \alpha^2)W_{xxxx} + W_{tt} - \frac{\alpha}{\gamma}Q_{xx} = r\Delta P. \tag{3.6}$$

In the latter, subscripts denote differentiation with respect to the relevant variable and

$$\alpha = \frac{\theta'}{\sqrt{B'C'}} \tag{3.7}$$

is a non-dimensional piezoelectric coupling parameter,

$$\beta = \frac{B'}{L'^3 I'_{\mathrm{b}} g} \tag{3.8}$$

is a non-dimensional stiffness,

$$r = \frac{\rho L'}{I'_{\mathrm{b}}} \tag{3.9}$$

is a surface density ratio and finally $\gamma = 1/\sqrt{\beta}$. Analogously, the non-dimensional forms of the electromechanical equation (3.3) and the circuit equation (3.4) are, respectively,

$$Q = V + \frac{\alpha}{\gamma}W_{xx} \tag{3.10}$$

and

$$V + \xi Q_t = 0, \tag{3.11}$$

where

$$\xi = \frac{C'}{G'}\sqrt{\frac{g}{L'}} \tag{3.12}$$

is a non-dimensional resistive term. Finally, the non-dimensional kinematic conditions at the ends of the plate (2.14) become

$$W(\pm 1, t) = W_x(x, t)|_{x=\pm 1} = 0. \tag{3.13}$$

Non-dimensionalization of the hydrodynamic equations (2.15)–(2.19) according to (3.5) yields, respectively,

$$\nabla^2 \Phi = 0 \tag{3.14}$$

for the Laplace equation in the fluid domain,

$$\Phi_{tt} + \Phi_z = 0, \quad z = 0, \tag{3.15}$$

for the kinematic–dynamic boundary condition on the free surface,

$$\frac{L'}{A'} z + P + \Phi_t = 0, \tag{3.16}$$

for the Bernoulli equation,

$$\Phi_z = 0, \quad z = -h, \tag{3.17}$$

for the bottom boundary condition and finally

$$W_t = \Phi_z, \quad |x| \le 1,\ z = -d \pm \delta, \quad \delta \to 0, \tag{3.18}$$

for the kinematic boundary condition on the plate.

Because the wave forcing is harmonic with frequency ω, time can be factored out by introducing the spatial variables

$$[\Phi(x, z, t), P(x, z, t), W(x, t), Q(x, t), V(x, t)] = \Re\{[\phi(x, z), p(x, z), w(x), q(x), v(x)]\, \mathrm{e}^{-\mathrm{i}\omega t}\}, \tag{3.19}$$

where i is the imaginary unit. In the following, the real part operator $\Re$ will be omitted for the sake of brevity. We shall now write the coupled boundary-value problem in terms of the spatial potential ϕ only. First, substitute (3.19) into the hydrodynamic equations (3.14), (3.15) and (3.17) to get the following system:

$$\nabla^2 \phi = 0, \quad \text{in fluid domain}, \tag{3.20}$$

$$\phi_z - \omega^2 \phi = 0, \quad z = 0 \tag{3.21}$$

and

$$\phi_z = 0, \quad z = -h. \tag{3.22}$$

Second, substitute the factorization (3.19) into the electromechanical equations (3.6), (3.10) and the Bernoulli equation (3.16). Then, couple them all together to get the following dynamic boundary condition on the plate,

$$\beta\left(1 + \frac{\alpha^2 \omega \xi}{\mathrm{i} + \omega \xi}\right)\phi_{xxxz} - \omega^2 \phi_z = \omega^2 r \Delta\phi, \quad |x| < 1, z = -d \pm \delta, \quad \delta \to 0, \tag{3.23}$$

where, accordingly, $\Delta\phi(x)$ is the jump of the spatial potential across the plate along the z-direction. Finally, substitute (3.19) into the end conditions (3.13) and the kinematic equation (3.18). Again, couple the equations together to obtain

$$\phi_z = \phi_{xz} = 0, \quad x = \pm 1,\ z = -d \pm \delta, \quad \delta \to 0. \tag{3.24}$$

The system (3.20)–(3.24) is now expressed in terms of the spatial potential ϕ only and will be solved with the method of matching potentials [20]. Note that, in the short-circuit limit $\xi \to 0$, the second term inside the brackets at the left-hand side of (3.23) vanishes. Within this limit,

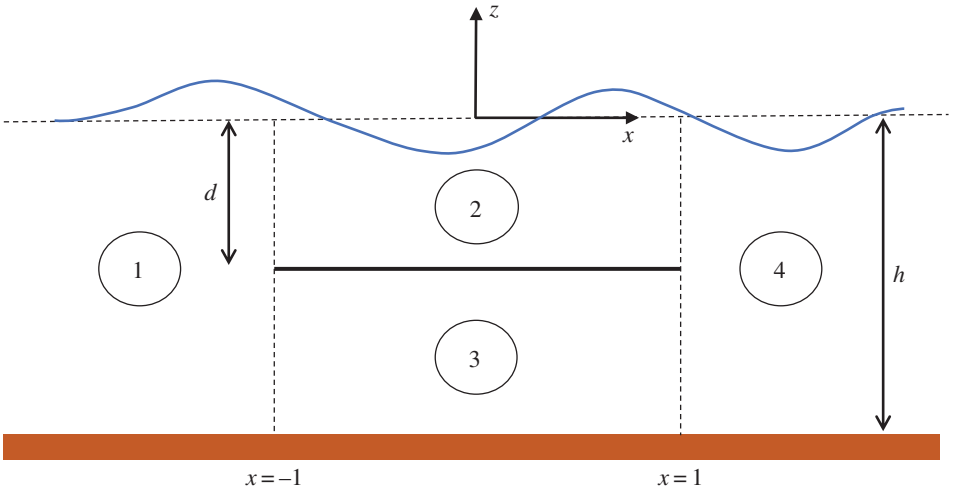

Figure 3. Domain decomposition used to solve the boundary-value problem (3.20)–(3.24). (Online version in colour.)

the fifth derivative of the velocity potential in (3.23) is multiplied only by the non-dimensional stiffness β and the resulting boundary-value problem is equivalent to that of a submerged elastic plate without power extraction [21–24], as expected. Indeed, the complex coefficient $\alpha^2\omega\xi/(\mathrm{i}+\omega\xi)$ in (3.23) is a dissipative term which models the extraction of energy from the system by means of the resistive circuits of figure 2.

The boundary-value problem (3.20)–(3.24) is now well-posed, as it consists of the governing partial differential equation (3.20) and appropriate conditions at each of the physical boundaries of the system. To find the solution, we follow [23,25] and split the fluid domain into four different areas, as shown in figure 3. The matching conditions at the common boundaries of the four domains are

$$\phi_{2z} = \phi_{3z}, \qquad |x| < 1,\ z = -d, \tag{3.25}$$

$$\phi_1 = \phi_2, \quad \phi_{1x} = \phi_{2x}, \quad x = -1,\ z \in (-d, 0), \tag{3.26}$$

$$\phi_1 = \phi_3, \quad \phi_{1x} = \phi_{3x}, \quad x = -1,\ z \in (-h, -d), \tag{3.27}$$

$$\phi_2 = \phi_4, \quad \phi_{2x} = \phi_{4x}, \quad x = 1,\ z \in (-d, 0) \tag{3.28}$$

and

$$\phi_3 = \phi_4, \quad \phi_{3x} = \phi_{4x}, \quad x = 1,\ z \in (-h, -d), \tag{3.29}$$

where the ϕ_i denote the potential ϕ in each area $i = 1, 2, 3, 4$. We also require that the scattered potentials in the open ocean areas 1 and 4 are outgoing in the far field [20]. We shall now solve the boundary-value problem separately in each region and then match the potentials via (3.25)–(3.29).

(a) Regions 1 and 4

The boundary-value problem for $\phi_1(x, z)$ is simply (3.20)–(3.22). The solution is the well-known superimposition of incident, reflected (left-going) and evanescent waves [20],

$$\phi_1(x, z) = -\frac{\mathrm{i}}{\omega}\frac{\cosh[k(z+h)]}{\cosh(kh)}\,\mathrm{e}^{\mathrm{i}kx} + \sum_{n=0}^{\infty} R_n\,\mathrm{e}^{-\mathrm{i}\kappa_n x} Z_n(z). \tag{3.30}$$

In the latter, the R_n are unknown complex coefficients, whereas $\kappa_0 = k$ and $\kappa_n = \mathrm{i}k_n$ are the solutions of the dispersion relation

$$\omega^2 = k\tanh(kh); \quad \omega^2 = -k_n\tan(k_n h). \tag{3.31}$$

Still in (3.30), the Z_n are the orthonormal functions

$$Z_n(z) = \frac{\sqrt{2}\cosh[\kappa_n(z+h)]}{(h+\omega^{-2}\sinh^2(\kappa_n h))^{1/2}}. \tag{3.32}$$

The latter satisfy $\int_{-h}^{0} Z_n Z_m \,\mathrm{d}z = \delta_{nm}$, where δ_{nm} is the Kronecker delta; see [5,20].

In region 4, the solution of the system (3.20)–(3.22) is the superimposition of a transmitted (right-going) wave and evanescent waves

$$\phi_4(x,z) = \sum_{n=0}^{\infty} T_n \,\mathrm{e}^{\mathrm{i}\kappa_n x} Z_n(z), \tag{3.33}$$

where the T_n are unknown complex coefficients.

(b) Regions 2 and 3

In region 2, the potential ϕ_2 must satisfy the Laplace equation (3.20) and the surface condition (3.21). In region 3, the potential ϕ_3 must still satisfy the Laplace equation (3.20), but with the bottom boundary condition (3.22). Furthermore, both ϕ_2 and ϕ_3 must satisfy the continuity condition (3.25). The solutions to this problem are

$$\phi_{(2,3)}(x,z) = \sum_{n=-2}^{\infty} (A_n \,\mathrm{e}^{\mathrm{i}\sigma_n x} + B_n \,\mathrm{e}^{-\mathrm{i}\sigma_n x})\psi_n^{(2,3)}(z), \tag{3.34}$$

where the A_n and B_n are unknown complex coefficients and

$$\psi_n^{(2)}(z) = [\sigma_n \cosh(\sigma_n z) + \omega^2 \sinh(\sigma_n z)]\sinh[\sigma_n(h-d)], \tag{3.35}$$

and

$$\psi_n^{(3)}(z) = [\omega^2 \cosh(\sigma_n d) - \sigma_n \sinh(\sigma_n d)]\cosh[\sigma_n(z+h)], \tag{3.36}$$

are the vertical eigenfunctions of the regions 2 and 3, respectively. Expression (3.34) corresponds to a system of forward- and backward-travelling waves (i.e. in regions 2 and 3 the radiation condition does not apply). Note that the starting index of the series in (3.34) has been chosen to be -2, for reasons that will become clear shortly. This choice is only practical and obviously does not affect the solution in any way. The σ_n in (3.34)–(3.36) are horizontal wavenumbers, still unknown. They are to be determined by substituting (3.34) into the boundary condition on the plate, expression (3.23). This operation yields a novel hydroelectromechanical dispersion relation:

$$\begin{aligned} F(\sigma_n) = {} & \left[\beta\left(1+\frac{\alpha^2\omega\xi}{\mathrm{i}+\omega\xi}\right)\sigma_n^4 - \omega^2\right][\omega^2\sigma_n\cosh(\sigma_n d) - \sigma_n^2\sinh(\sigma_n d)]\tanh[\sigma_n(h-d)] \\ & - \omega^2 r\{\omega^2\cosh(\sigma_n d) - \sigma_n\sinh(\sigma_n d) + [\omega^2\sinh(\sigma_n d) - \sigma_n\cosh(\sigma_n d)] \\ & \times \tanh[\sigma_n(h-d)]\} = 0. \end{aligned} \tag{3.37}$$

The latter expression is an even complex function of σ_n and admits an infinite number of complex solutions $\pm\sigma_n$. Because each of these pairs correspond to the same eigenfunction $\psi_n^{(2,3)}$ (see (3.35)–(3.36)) from now on we will consider only the solutions σ_n lying in the first and fourth quadrants of the complex plane, discarding their repetitions in the second and third quadrants. Before proceeding to the calculation of the unknown parameters R_n, T_n, A_n and B_n, we analyse the properties of the dispersion relation (3.37) in more detail.

(c) Properties of the hydroelectromechanical dispersion relation

First, note that in the short-circuit limit $\xi \to 0$, the hydroelectromechanical equation (3.37) coincides with the dispersion relation of a submerged elastic plate studied by Hassan & Meylan [23]. Within this limit, (3.37) is known to admit two complex roots, say σ_{-2} and σ_{-1},

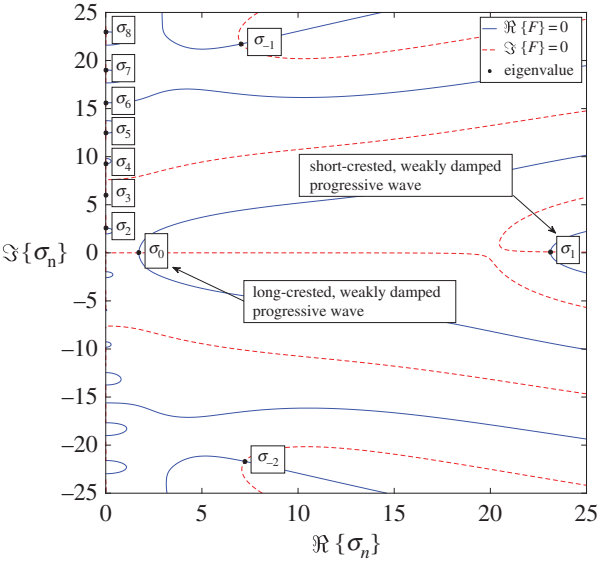

Figure 4. Location of the first 11 eigenvalues of the hydroelectromechanical dispersion relation $F(\sigma_n) = 0$ in the complex σ_n plane, see (3.37). The solid blue lines identify the contours $\Re\{F\} = 0$, whereas the dashed red lines correspond to the contours $\Im\{F\} = 0$. The parameters are $\alpha = 0.21$, $\beta = 3.8 \times 10^{-4}$ and $\xi = 1$. (Online version in colour.)

two positive real roots, say σ_0 and σ_1, and an infinite number of positive imaginary roots σ_n, $n = 2, 3, \ldots$, for typical plate parameters [23]. Now, the presence of the complex piezoelectric term proportional to ξ in (3.37) changes the location of the roots of the dispersion relation in the complex plane, with respect to the short-circuit scenario. Figure 4 shows the location of the complex roots of the hydroelectromechanical dispersion relation (3.37) for a typical system configuration. In this example, the wave period is $T' = 5\,\mathrm{s}$, the length of the plate is $2L' = 20\,\mathrm{m}$, the water depth is $h' = 10\,\mathrm{m}$ and the submergence of the plate is $d' = 2\,\mathrm{m}$. The substrate is made of silicone rubber and the piezoelectric layers are made of polyvinylidene fluoride (PVDF). The rubber layer has thickness $d'_0 = 0.01\,\mathrm{m}$ and each of the piezoelectric layers have thickness $d'_\mathrm{p} = 1.1 \times 10^{-4}\,\mathrm{m}$; see [26]. Typical values of the system coefficients for commercial silicone rubber and PVDF are $\alpha \simeq 0.21$, $\beta \simeq 3.8 \times 10^{-4}$ and $\xi \simeq 1$ [8,15,27]. In this paper, we have determined the roots of the hydroelectromechanical dispersion relation (3.37) with a two-dimensional Newton–Raphson method of tolerance $\epsilon = 10^{-9}$; see [28]. The numerical values of the complex roots shown in figure 4 are reported in table 1. As for the submerged elastic plate, there are still two roots in the complex plane, which we name σ_{-2} and σ_{-1}, following [23,25]. These roots correspond to non-propagating modes, as discussed by Behera & Sahoo [25]. Furthermore, table 1 reveals that (3.37) admits no real roots. The effect of the piezoelectric term in (3.37) is to slightly shift σ_0 and σ_1 into the first quadrant of the complex plane. Because the imaginary part (damping rate) of such wavenumbers is very small, physically they correspond to weakly damped progressive waves. Finally, table 1 also reveals that (3.37) has no imaginary roots. Again, the effect of the piezoelectric term with respect to the short-circuit scenario is to shift the σ_n into the first quadrant. As a result, there is an infinite number of complex solutions σ_n, $n = 2, 3, \ldots$ whose real part is much smaller than the imaginary part (see again table 1). These modes physically describe evanescent waves.

Such a physical picture is reminiscent of that of submerged breakwater porous structures; see [25,29]. Indeed, mathematically the piezoelectric term in (3.37) has a similar role as the porous-effect parameter of Behera & Sahoo [25]. However, the similarity is only formal, because of the substantially different nature and magnitude of such terms. For example, the roots σ_0 and σ_1 of Behera & Sahoo [25] are characterized by a significant imaginary part. This of course ensures that the structural porosity of the breakwater dissipates a substantial amount of energy. On the

Table 1. Numerical values of the complex eigenvalues σ_n, solutions of the dispersion relation (3.37), represented in figure 4. The numerical tolerance of the Newton–Raphson scheme is $\epsilon = 10^{-9}$.

Eigenvalue	numerical value	behaviour in the plate region
σ_{-2}	$7.2318 - 21.6916\mathrm{i}$	non-propagating
σ_{-1}	$7.05261 + 21.7312\mathrm{i}$	non-propagating
σ_0	$1.7188 + 6 \times 10^{-8}\mathrm{i}$	long-crested weakly damped
σ_1	$23.1267 + 0.0957\mathrm{i}$	short-crested weakly damped
σ_2	$7 \times 10^{-7} + 2.5814\mathrm{i}$	evanescent
σ_3	$5 \times 10^{-5} + 6.0166\mathrm{i}$	evanescent
σ_4	$0.0003 + 9.2601\mathrm{i}$	evanescent
σ_5	$0.0005 + 12.4574\mathrm{i}$	evanescent
σ_6	$4 \times 10^{-5} + 15.6069\mathrm{i}$	evanescent
σ_7	$0.0043 + 19.0077\mathrm{i}$	evanescent
σ_8	$0.0109 + 22.9781\mathrm{i}$	evanescent

other hand, in the present case, the wavenumbers σ_0 and σ_1 have a small imaginary part (table 1), which means that their horizontal decay is weaker than that of the porous plate case. This scenario corresponds to waves that traverse the device and trigger the piezoelectric effect on the plate, which in turn dampens the wave height. Furthermore, note from table 1 that $\Re\{\sigma_1\} \gg \Re\{\sigma_0\}$. Because the real part of the wavenumber is related to the propagating part of the perturbation, the latter inequality means that σ_1 and σ_0 correspond, respectively, to short- and long-crested waves (see again figure 4). This does not happen in the flexible plate case of Hassan & Meylan [23] and in the porous plate case of [25], where the two wavenumbers are comparable. Therefore, the occurrence of a coupled system of short- and long-crested weakly damped progressive waves that propagate in the plate region is a distinctive feature of the submerged piezoelectric plate. We will show later that the short-crested wave component is responsible for the resonant enhancement of the power generated by the device; see §5.

(d) Numerical solution

Having solved the dispersion relation (3.37), we are now in a position to find the numerical values of the amplitude coefficients A_n, B_n, R_n and T_n. First, substitute the solutions ϕ_1 (3.30), ϕ_2 and ϕ_3 (3.34) into the first conditions of both (3.26) and (3.27). Then, multiply both equations by $Z_m(z)$, $m = 0, 1, \ldots$, integrate them along z over the respective domains and finally sum the results to obtain

$$R_m = \frac{\mathrm{i}}{\omega} \mathrm{e}^{-\mathrm{i}(k+\kappa_m)} a_m \delta_{0m} + \sum_{n=-2}^{N} [A_n \mathrm{e}^{-\mathrm{i}(\sigma_n+\kappa_m)} + B_n \mathrm{e}^{\mathrm{i}(\sigma_n-\kappa_m)}] b_{mn}, \quad m = 0, 1, \ldots, N. \tag{3.38}$$

In the latter, the orthogonality of the vertical modes Z_m has been exploited and the sum has been truncated to a finite value $n = N$ for numerical evaluation. Still in (3.38),

$$a_m = \int_{-h}^{0} \frac{\cosh[k(z+h)]}{\cosh(kh)} Z_m(z)\, \mathrm{d}z \tag{3.39}$$

and

$$b_{mn} = \int_{-d}^{0} \psi_n^{(2)}(z) Z_m(z)\, \mathrm{d}z + \int_{-h}^{-d} \psi_n^{(3)}(z) Z_m(z)\, \mathrm{d}z \tag{3.40}$$

are complex coefficients. Using the same procedure to match the fluxes (second conditions of both (3.26) and (3.27)) gives

$$\sum_{n=-2}^{N}[A_n\,\mathrm{e}^{-\mathrm{i}\sigma_n}(\sigma_n+\kappa_m)-B_n\,\mathrm{e}^{\mathrm{i}\sigma_n}(\sigma_n-\kappa_m)]b_{nm}=-\frac{\mathrm{i}}{\omega}(k+\kappa_m)\,\mathrm{e}^{-\mathrm{i}k}a_m\delta_{0m},\quad m=0,1,\ldots N. \tag{3.41}$$

Finally, matching potentials and fluxes at the common boundary between regions 3 and 4 (see equations (3.28) and (3.29)) yields

$$T_m=\sum_{n=-2}^{N}[A_n\,\mathrm{e}^{\mathrm{i}(\sigma_n-\kappa_m)}+B_n^{-\mathrm{i}(\sigma_n+\kappa_m)}]b_{mn},\quad m=0,1,\ldots,N, \tag{3.42}$$

and

$$\sum_{n=-2}^{N}[A_n\,\mathrm{e}^{\mathrm{i}\sigma_n}(\sigma_n-\kappa_m)-B_n\,\mathrm{e}^{-\mathrm{i}\sigma_n}(\sigma_n+\kappa_m)]b_{mn}=0,\quad m=0,1,\ldots,N. \tag{3.43}$$

Expressions (3.41) and (3.43) are $2(N+1)$ equations in $2(N+3)$ unknowns, namely the A_n and B_n, $n=-2,-1,\ldots,N$. Hence, we need four additional equations to close the system. These are readily provided by the clamping conditions on the plate (3.24), which we have not used yet. Substitution of either ϕ_2 or ϕ_3 into (3.24) gives the following four equations:

$$\sum_{n=-2}^{N}(A_n\,\mathrm{e}^{-\mathrm{i}\sigma_n}+B_n\,\mathrm{e}^{\mathrm{i}\sigma_n})\mathcal{F}_n=0, \tag{3.44}$$

$$\sum_{n=-2}^{N}(A_n\,\mathrm{e}^{\mathrm{i}\sigma_n}+B_n\,\mathrm{e}^{-\mathrm{i}\sigma_n})\mathcal{F}_n=0, \tag{3.45}$$

$$\sum_{n=-2}^{N}(A_n\sigma_n\,\mathrm{e}^{-\mathrm{i}\sigma_n}-B_n\sigma_n\,\mathrm{e}^{\mathrm{i}\sigma_n})\mathcal{F}_n=0 \tag{3.46}$$

and

$$\sum_{n=-2}^{N}(A_n\sigma_n\,\mathrm{e}^{\mathrm{i}\sigma_n}-B_n\sigma_n\,\mathrm{e}^{-\mathrm{i}\sigma_n})\mathcal{F}_n=0, \tag{3.47}$$

where

$$\mathcal{F}_n=[\omega^2\cosh(\sigma_n d)-\sigma_n\sinh(\sigma_n d)]\sigma_n\sinh[\sigma_n(h-d)]. \tag{3.48}$$

The system (3.41), (3.43)–(3.48) can now be solved numerically for the A_n and B_n with a suitable choice of N. Details on the numerical convergence of the system are given in appendix A. Once the A_n and B_n are known, the R_n and T_n can be found directly with (3.38) and (3.42), respectively.

4. Plate motion and wave power extraction

Having solved numerically the boundary-value problem for the potential, we can easily determine all the remaining quantities of engineering interest. First, define the free-surface elevation $z'=\zeta'(x',t')=A'\zeta(x,t)$, so that $\zeta_t=\Phi_z|_{z=0}$; see [20]. Then, factor time out by defining $\zeta(x,t)=\Re\{\eta(x)\,\mathrm{e}^{-\mathrm{i}\omega t}\}$. Hence

$$\eta_i(x)=\frac{\mathrm{i}}{\omega}\phi_{i_z}(x,z)|_{z=0},\quad i=1,2,4 \tag{4.1}$$

is the spatial component of the free-surface elevation in the region $i = 1, 2, 4$. Substituting the relevant forms for the potentials (3.30)–(3.33) into (4.1), we obtain the reflection coefficient in region 1,

$$R = \frac{\mathrm{i}}{\omega} R_0 \frac{\sqrt{2}k \sinh(kh)}{[h + \omega^{-2} \sinh^2(kh)]}, \tag{4.2}$$

and the transmission coefficient in region 4,

$$T = \frac{\mathrm{i}}{\omega} T_0 \frac{\sqrt{2}k \sinh(kh)}{[h + \omega^{-2} \sinh^2(kh)]}, \tag{4.3}$$

see [20]. Combining (3.18), (3.19) and (3.34), we obtain the spatial displacement of the plate

$$w(x) = \frac{\mathrm{i}}{\omega} \sum_{n=-2}^{N} (A_n \, \mathrm{e}^{\mathrm{i}\sigma_n x} + B_n \, \mathrm{e}^{-\mathrm{i}\sigma_n x}) \mathcal{F}_n. \tag{4.4}$$

Concerning the energy budget of the device, the rate of mechanical energy flux is $W'_m = W'_\mathrm{p} - W'_\mathrm{el} - \mathcal{P}'$, where W'_p is the rate of work of the fluid force on the plate, W'_el is the rate of electrical energy flux and $\mathcal{P}'$ is the electric power available in the output system per unit width (see [16]). The latter is given by

$$\mathcal{P}' = -\int_{-L'}^{L'} V' \frac{\partial Q'}{\partial t'} \, \mathrm{d}x'. \tag{4.5}$$

Using Ohm's law (2.13) and integrating over the length of the device and over a period $T' = 2\pi/\omega'$, we obtain the average power

$$\bar{\mathcal{P}}' = \frac{(A'g)^2}{L'} \frac{I'_\mathrm{b} C'}{G'} \bar{\mathcal{P}}, \tag{4.6}$$

in W m^{-1}, where

$$\bar{\mathcal{P}} = \int_{-1}^{1} \left[\frac{1}{T} \int_0^T Q_t^2(x, t) \, \mathrm{d}t \right] \mathrm{d}x \tag{4.7}$$

is the non-dimensional average power extracted by the device per unit width over a cycle. Note that this results yields only if the patches are designed, so that voltage cancellations do not occur along the plate; see [8]. Finally, substitute (3.10)–(3.11) into (4.7) and factor time out with (3.19). Calculation of the inner integral, using the property $1/T \int_0^T \Re\{A \, \mathrm{e}^{-\mathrm{i}\omega t}\} \Re\{B \, \mathrm{e}^{-\mathrm{i}\omega t}\} \, \mathrm{d}t = 1/2 \Re\{AB^*\}$ gives

$$\bar{\mathcal{P}} = \frac{\omega^2}{2} \int_{-1}^{1} \left| \frac{\alpha w_{xx}}{\gamma(1 - \mathrm{i}\omega\xi)} \right|^2 \mathrm{d}x, \tag{4.8}$$

for the non-dimensional average power per unit width of the device. For a resistive circuit in permanent periodic regime, Michelin & Doaré [16] have shown that $\bar{W}_\mathrm{p} = \bar{\mathcal{P}}$.

5. Discussion

In this section, we analyse the dynamics of wave power extraction for a typical plate configuration. As in §3, the length of the plate is $2L' = 20$ m, the water depth is $h' = 10$ m and the submergence of the plate is $d' = 2$ m. The rubber layer has thickness $d'_0 = 0.01$ m and each of the piezoelectric layers have thickness $d'_\mathrm{p} = 1.1 \times 10^{-4}$ m. The system parameters for silicone rubber (substrate) and PVDF (piezoelectric layers) are $\alpha = 0.21$, $\beta = 3.8 \times 10^{-4}$ and $\xi = 1$.

(a) Piezoelectric plate dynamics and wave power extraction

Figure 5 shows a snapshot of the system with the displacements $w'(x', t')$ of the flexible piezoelectric plate and the free-surface elevation $\zeta'(x', t')$. The ocean surface waves have amplitude $A' = 1$ m and period $T' = 5$ s, corresponding to a wavelength $\lambda' = 36.58$ m. Note that the free surface matches seamlessly across the regions defined in §3 and that the clamping conditions

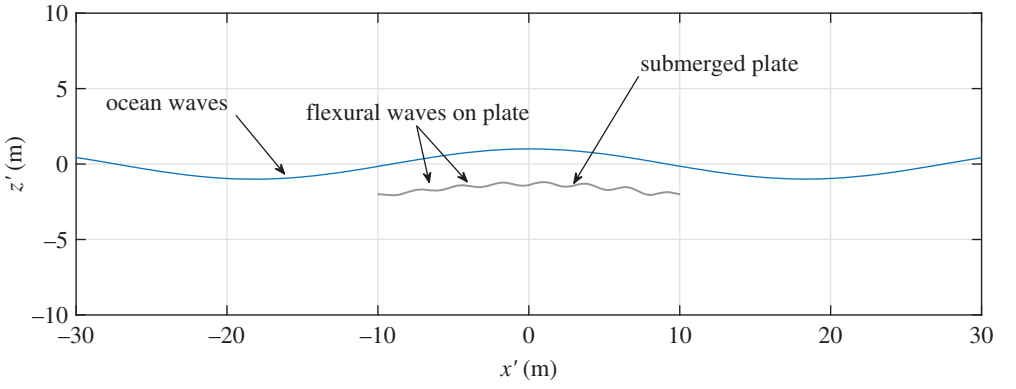

Figure 5. Snapshot of the free-surface elevation $\zeta'(x', t')$ and plate displacements $w'(x', t')$ at time $t' = T'$. Parameters are: $A' = 1$ m, $T' = 5$ s, $\alpha = 0.21$, $\beta = 3.8 \times 10^{-4}$ and $\xi = 1$. The first 12 flexural plate modes have been considered. (Online version in colour.)

on the plate, i.e. absence of displacements and rotations, are correctly satisfied by the numerical solution. On the plate, weakly damped progressive waves superimpose to create short-crested oscillations of wavelength $\lambda'_1 = 2\pi L'/\Re\{\sigma_1\}$, slowly modulated by a long-crested oscillation of wavelength $\lambda'_0 = 2\pi L'/\Re\{\sigma_0\}$. In this example, $\lambda'_1 = 2.79$ m and $\lambda'_0 = 36.55$ m, which is very close to the wavelength λ' of the incident wave. The physical picture is hence clear. Owing to the coupled hydroelectromechanical effect, the incident wave is able to excite a coupled system of long- and short-crested weakly damped flexural waves. On the one hand, the long-crested component propagates essentially with the same wavelength and phase speed $c'_0 = \lambda'_0/T' = 7.31\,\mathrm{m\,s^{-1}}$ of the incoming wave. On the other hand, the short-crested waves travel at a much smaller wavelength and speed $c'_1 = 0.56\,\mathrm{m\,s^{-1}}$ than that of the forcing waves.

While the zeroth-mode long-crested component is the direct effect of the incident wave forcing, the nature of the first-mode short-crested wave is more puzzling. To gain a better physical insight into it, let us consider again the hydroelectromechanical dispersion relation and derive its asymptotic form for short waves. The short-wave limit of (3.37) when $\Re\{\sigma_n\} \gg 1$ yields the following approximation for the first-mode wavenumber:

$$\sigma_1 \sim \left[\frac{2\omega^2 r}{\beta(1+\alpha^2\omega\xi/(\mathrm{i}+\omega\xi))}\right]^{1/5}. \tag{5.1}$$

For our sample system, the asymptotic approximation (5.1) gives $\sigma_1 \sim 23.0598 + 0.0952\mathrm{i}$, which indeed is very close to the value of σ_1 shown in table 1. Expression (5.1) reveals that the first-mode short-crested flexural wave is the effect of the hydroelectromechanical coupling, sustained by the density difference at the water–plate interface. Note also that the smaller the stiffness of the plate β, the greater is σ_1 and the shorter is the wavelength λ'_1 of the first-mode flexural wave.

Let us now investigate the effect of the incident period on the generated power. Figure 6 shows the behaviour of the average extracted power (4.7) with respect to the period of the incident waves, for the sample piezoelectric plate studied in this section. The plot of figure 6 reveals the existence of resonant periods at which the extracted power is significant, with a maximum peak of about 4.4 kW at $T' \simeq 5.4$ s. Note that this value is about two orders of magnitude greater than the power output of piezoelectric beams predicted by simplified uncoupled models [9–11]. Clearly, the presence of sharp resonant peaks in the generated power is due to the coupled hydroelectromechanical behaviour of the device. This is studied in detail in the following section.

(i) Resonance

Let us now analyse the resonant periods of figure 6, at which the power capture curve shows local peaks. Note that the average extracted power depends on the square of the plate curvature,

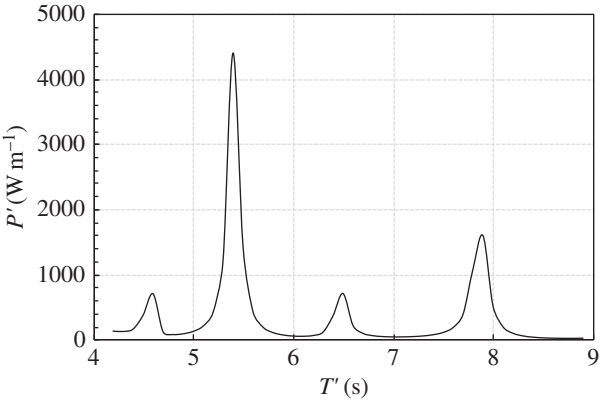

Figure 6. Wave power generated by a bimorph piezoelectric plate WEC of length $2L' = 20$ m and submergence $d' = 2$ m in water depth $h' = 10$ m, versus the period of the incident wave. The parameters are: $A' = 1$ m, $\alpha = 0.21$, $\beta = 3.8 \times 10^{-4}$ and the resistive term is $\xi = 1$. The first 13 modes have been considered.

see (4.8). Hence, the short-crested component ($n = 1$) of the flexural waves (3.34) makes a leading contribution to the overall power capture of the system. As a consequence, we expect that the plate resonates when the wavelength of the first-mode flexural waves is close to one of the wavelengths of natural vibration of the plate. Physically, the natural vibrations are the solutions of the problem in which the plate performs free oscillations without damping. In our system, damping is associated with the PTO system and with the reflected and transmitted waves in regions 1 and 4, respectively. Therefore, to study undamped oscillations we must analyse the system in short-circuit condition ($\xi = 0$) and without surrounding water ($r = 0$). The governing equation for the flexural waves on the plate (3.23) becomes then

$$\beta w_{xxxx} - \omega^2 w = 0, \quad |x| < 1, z = -d \pm \delta, \quad \delta \to 0, \tag{5.2}$$

where $w(x) = (\mathrm{i}/\omega)\,\phi_{2z}|_{z=-d}$ is the spatial displacement of the plate (see (2.19) and (3.19)). In addition, the clamping conditions (3.24) give $w = w_x = 0$ at $x = \pm 1$. This yields a Stürm–Liouville problem whose general solution

$$w = A\cos(\mu x) + B\sin(\mu x) + C\cosh(\mu x) + D\sinh(\mu x)$$

admits the eigenvalues

$$\mu = \mu_{\mathrm{p}} \simeq \left(p + \frac{1}{2}\right)\frac{\pi}{2}, \quad p = 1, 2, \ldots, \tag{5.3}$$

see [17]. Equating the latter expression to the approximated analytical form of the first-mode flexural wavenumber (5.1) in short-circuit conditions ($\xi = 0$), we obtain an approximated expression for the resonant periods of the system,

$$T'_{\mathrm{p}} \simeq 16\sqrt{\frac{rL'}{(p + 1/2)^5 \pi^3 g\beta}}, \quad p = 1, 2, \ldots \tag{5.4}$$

where (3.5) has been used to express the result in physical variables. In reality, we expect the resonant periods to be slightly greater than (5.4) because of the presence of dissipations owing to both radiation damping and wave energy extraction in the full problem; see [20]. The resonant periods predicted by the approximated formula (5.4) are reported in table 2 together with the actual values. The good agreement between the two sets of data confirms that the short-crested component of the flexural waves travelling on the plate is responsible for the resonant behaviour of the converter. Note that the resonant periods (5.4) are directly proportional to the density ratio r and the length of the device L', and inversely proportional to the stiffness of the system β. Therefore, such parameters could be optimized to make the device resonate with

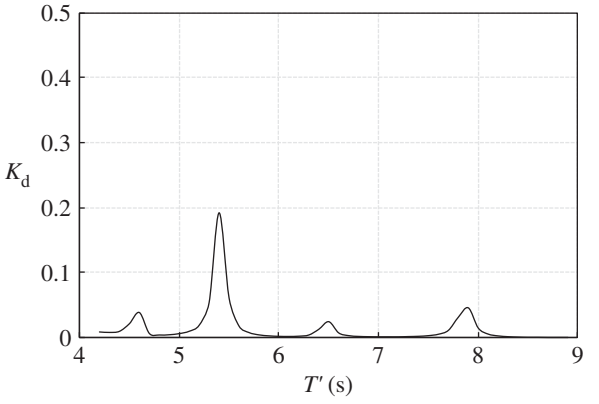

Figure 7. Damping coefficient (5.5) versus period of the incident wave. The parameters are the same as those of figure 6.

Table 2. Resonant periods of the system in the interval (4, 9) s and approximated values obtained with (5.4).

resonant period (s)	approximated value (s)
4.6	4.4
5.4	5.2
6.5	6.2
7.9	7.6

the most energetic sea states in a given ocean sector. We are currently investigating random sea optimization techniques.

(b) Wave damping

We have anticipated in §1 that the piezoelectric plate WEC can also be an effective damper. In this section, we investigate the wave damping capacity of the device in more detail. Following Behera & Sahoo [25], define the dissipation coefficient as

$$K_d = 1 - |R|^2 - |T|^2, \tag{5.5}$$

where R and T are given, respectively, by (4.2) and (4.3). Figure 7 shows the behaviour of the dissipation coefficient K_d versus the period of the incident wave, in physical variables. Normally, the plate is able to reduce the amplitude of the surrounding waves only by a small proportion. However, if the plate is designed to resonate, energy dissipation increases and the damping effect of the plate can become significant. For the sample plate studied in this paper, the maximum damping coefficient is 20% at the resonant period $T' = 5.4$ s, see again figure 7. This makes the piezoelectric plate WEC a versatile device, which can provide a useful damping action around offshore oil platforms or in combination with near shore breakwaters.

6. Conclusion

We have derived a fully coupled model of a piezoelectric plate wave energy converter. The semi-analytical solution of the problem was obtained by coupling a distributed-parameter model of the piezoelectric system with a potential-flow model of the water waves.

A novel hydroelectromechanical dispersion relation was obtained and solved in the complex wavenumber plane. The solution showed the existence of a coupled system of short- and long-crested weakly damped flexural waves in the plate region. As a consequence of this dynamics, the

plate is forced to vibrate in short-crested oscillations slowly modulated by the long-crested wave. We showed that the short-crested component is responsible for the occurrence of resonant peaks in the power production of the device. At resonance, the system can extract a significant amount of energy, which can be used for low-power applications such as supplying LEDs, wireless routers, computers, sensors, etc. Finally, we showed that the piezoelectric device can act as a good wave energy damper when it resonates with the incident waves.

We made several simplifying assumptions to develop the mathematical model. First, we neglected the influence of the supporting structure of the plate on the wave field. In reality, a number of vertical struts would need to be used to support the clamps. These might have an effect on the wave field, which could be analysed with computational fluid dynamics (CFD) software. Second, we neglected the presence of voltage cancellations in the short-wave vibration mode of the plate. We remark that the present model is valid only if the length scale of the plate deformation is greater than the length of each patch, i.e. $\lambda_1 > \mathrm{d}X$. If this assumption is violated, voltage cancellations may occur; see Jbaily & Yeung [4]. In that case, one must use segmented electrodes to avoid cancellation, which would then require the definition of separate voltage terms, as described by Ertuk & Inman [8]. Third, in the case of obliquely incident waves, three-dimensional effects could become relevant and would need to be modelled appropriately. We are currently developing a full numerical model based on a finite-element approximation of the boundary-value problem. This can be easily extended to handle arbitrary geometrical shapes of the plate in three dimensions. However, we emphasize that the semi-analytical model developed in this paper offers a valuable physical insights into the problem, which the numerical model cannot provide.

Mathematically, we solved the coupled hydroelectromechanical boundary-value problem using separation of variables and the method of matching potentials, as in [23,25]. Hassan & Meylan [23] already pointed out that the eigenfunction-matching method does not have optimal convergence rates because of the singularity at the plate tip. However, more analytic approaches such as the Wiener–Hopf technique or the residue calculus method require structures of semi-infinite length along the x-axis [23], and so could not be applied to this study. Note also that the analysis was performed in the framework of a linearized theory for both the plate deformation and the wave motion. Close to resonance, the displacements of the plate might become significant and a nonlinear analysis should be carried out to refine the power output predictions.

Our current research efforts are oriented towards determining the parametric behaviour of the system in order to find optimal device configurations. Owing to the large number of parameters (e.g. α, β, ξ, ω, d, h, r, etc.) and the large extent of the parametric space, we are using genetic algorithms to map the parametric behaviour of the system and identify areas of high-quality solutions in the space of parameters. This will allow us to obtain a database of possible PWEC configurations of interest to the wave energy industry.

Data accessibility. The key data to fully reproduce the results of this work are presented in tables 1 and 2.

Competing interests. I declare I have no competing interests.

Funding. This research received no specific external funding. Internal funding from the School of Science, Loughborough University is kindly acknowledged.

Acknowledgements. Fruitful discussions with Dr Maureen McIver are kindly acknowledged. The analytical calculations have been validated by the skilful PhD student F. Buriani.

Appendix A

In this section, we provide some details on the numerical solution of the coupled hydroelectromechanical model of §3. The model is based on the solution of the linear system of equations (3.41), (3.43)–(3.48). This is achieved numerically by truncating the series expansions up to a suitable number of terms, N. To determine an appropriate value for N in our numerical calculations, we performed a convergence test by analysing the influence of N on the reflection and transmission coefficients of the system, respectively, (4.2) and (4.3). To assess convergence, we used the combined tolerance test [30], in which the error at the nth numerical iteration is

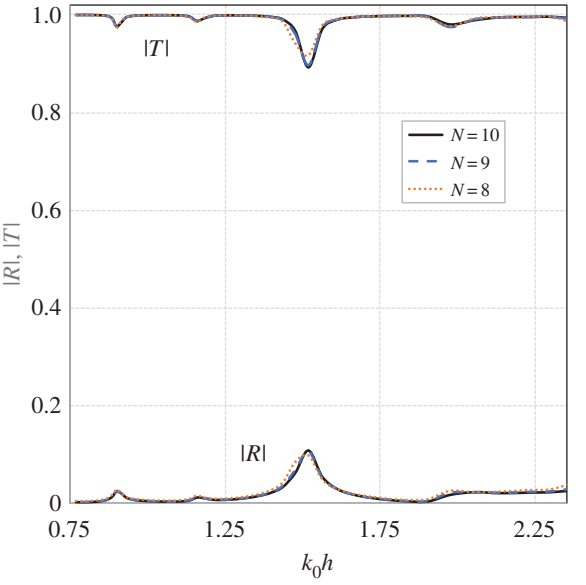

Figure 8. Behaviour of the transmission (top line) and reflection (bottom line) coefficients with respect to the non-dimensional parameter k_0h, for three different values of N. The maximum combined error for $N = 9$ is $O(10^{-3})$. (Online version in colour.)

calculated as

$$\epsilon_n = \frac{|x_{n+1} - x_n|}{\max\{1, |x_{n+1}|, |x_n|\}}. \tag{A 1}$$

In the latter, x_n is the value of the assessed quantity (either R or T) at the nth numerical iteration. Already with $N = 8$ the error ϵ_N is of the order $O(10^{-2})$ and decreases to $O(10^{-3})$ with $N = 9$. The latter is accurate enough for graphical purposes in all cases considered here. Figure 8 shows the behaviour of the absolute values of the transmission and reflection coefficients versus the non-dimensional parameter k_0h, for three different values of N. Note that there is practically no visible difference between the cases $N = 9$ and $N = 10$, so that $N = 9$ provides an adequate level of convergence. That corresponds to considering up to 12 flexural modes on the plate, $n = -2, -1, \ldots, 9$.

References

1. BBC News. 2014 Jobs go after no buyer found for Pelamis wave business. See http://www.bbc.co.uk/news/uk-scotland-scotland-business-30560980.
2. Aquamarine Power. 2015 Aquamarine Power ceases trading. See http://www.aquamarinepower.com/news/aquamarine-power-ceases-trading.aspx.
3. Magagna D, Uihlein A. 2014 *JRC ocean energy status report*. Luxembourg: European Union.
4. Jbaily A, Yeung RW. 2015 Piezoelectric devices for ocean energy: a brief survey. *J. Ocean Eng. Mar. Energy* **1**, 101–118. (doi:10.1007/s40722-014-0008-9)
5. Renzi E, Dias F. 2012 Resonant behaviour of an oscillating wave energy converter in a channel. *J. Fluid Mech.* **701**, 482–510. (doi:10.1017/jfm.2012.194)
6. Renzi E, Dias F. 2013 Hydrodynamics of the oscillating wave surge converter in the open ocean. *Eur. J. Mech. B, Fluid* **41**, 1–10. (doi:10.1016/j.euromechflu.2013.01.007)
7. Renzi E, Doherty K, Henry A, Dias F. 2014 How does oyster work? The simple interpretation of oyster mathematics. *Eur. J. Mech. B Fluid* **47**, 124–131. (doi:10.1016/j.euromechflu.2014.03.007)
8. Erturk A, Inman DJ. 2011 *Piezoelectric energy harvesting*. Chichester, UK: John Wiley & Sons, Ltd.
9. Xie XD, Wang Q, Wu N. 2014 Potential of a piezoelectric energy harvester from sea waves. *J. Sound Vib.* **333**, 1421–1429. (doi:10.1016/j.jsv.2013.11.008)

10. Xie XD, Wang Q, Wu N. 2014 Energy harvesting from transverse ocean waves by a piezoelectric plate. *Int. J. Eng. Sci.* **81**, 41–48. (doi:10.1016/j.ijengsci.2014.04.003)
11. Wu N, Wang Q, Xie XD. 2015 Ocean wave energy harvesting with a piezoelectric coupled buoy structure. *Appl. Ocean Res.* **50**, 110–118. (doi:10.1016/j.apor.2015.01.004)
12. Koola P, Ibragimov A. 2003 The dynamics of wave carpet - a novel deep water wave energy design. In *Oceans 2003. Celebrating the Past ... Teaming Toward the Future*, vol. 4, pp. 2288–2293. San Diego, CA: IEEE.
13. Franklin B, Brownrigg W, Farish M. 1774 On the stilling of waves by means of oil. Extracted from Sundry Letters between Benjamin Franklin, LL.D.F.R.S. William Brownrigg, M.D.F.R.S. and the Reverend Mr. Farish. *Phil. Trans.* **64**, 445–460. (doi:10.1098/rstl.1774.0044)
14. Lamb H. 1945 *Hydrodynamics*. New York, NY: Dover Publications.
15. Doaré O, Michelin S. 2011 Piezoelectric coupling in energy-harvesting fluttering flexible plates: linear stability analysis and conversion efficiency. *J. Fluid Struct.* **27**, 1357–1375. (doi:10.1016/j.jfluidstructs.2011.04.008)
16. Michelin S, Doaré O. 2013 Energy harvesting efficiency of piezoelectric flags in axial flows. *J. Fluid Mech.* **714**, 489–504. (doi:10.1017/jfm.2012.494)
17. Reddy JN. 2006 *Theory and analysis of elastic plates and shells*. London, UK: CRC, Taylor & Francis.
18. Sadiku MNO. 2001 *Elements of electromagnetics*. New York, NY: Oxford University Press.
19. Bisegna P, Caruso G, Maceri F. 2006 Optimized electric networks for vibration damping of piezoactuated beams. *J. Sound Vib.* **289**, 908–937. (doi:10.1016/j.jsv.2005.02.045)
20. Mei CC, Stiassnie M, Yue DK-P. 2005 *Theory and applications of ocean surface waves*. Singapore: World Scientific.
21. Wang CD, Meylan MH, Porter R. 2007 The linear wave response of a periodic array of floating elastic plates. *J. Eng. Math.* **57**, 23–40. (doi:10.1007/s10665-006-9054-1)
22. Evans DV, Porter R. 2008 Flexural waves on a pinned semi-infinite thin elastic plate. *Wave Motion* **45**, 745–757. (doi:10.1016/j.wavemoti.2007.11.006)
23. Hassan MU, Meylan MH. 2009 Water-wave scattering by submerged elastic plates. *Q. J. Mech. Appl. Math.* **62**, 321–344. (doi:10.1093/qjmam/hbp008)
24. Porter R. 2015 Linearised water wave problems involving submerged horizontal plates. *Appl. Ocean Res.* **50**, 91–109. (doi:10.1016/j.apor.2014.07.013)
25. Behera H, Sahoo T. 2015 Hydroelastic analysis of gravity wave interaction with submerged horizontal flexible porous plate. *J. Fluid Struct.* **54**, 643–660. (doi:10.1016/j.jfluidstructs.2015.01.005)
26. Measurement Specialities Inc. Piezo Film Sensors Technical Manual. Hampton, VA.
27. Tanaka Y, Oko T, Mutsuda H, Patel R, McWilliam S, Popov A. 2015 An experimental study of wave power generation using a flexible piezoelectric device. *J. Ocean Wind Energy* **2**, 28–36.
28. Press WH, Teukolsky SA, Vetterling WT, Flannery BP. 2007 *Numerical recipes*. New York, NY: Cambridge University Press.
29. McIver P. 1998 The dispersion relation and eigenfunction expansion for water waves in a porous structure. *J. Eng. Maths* **34**, 319–334. (doi:10.1023/A:1004389503576)
30. Ericson C. 2005 *Real-time collision detection*. London, UK: CRC, Taylor & Francis.